Thin–Walled Structures 192 (2023) 111123

Contents lists available at ScienceDirect

Thin-Walled Structures

journal homepage: www.elsevier.com/locate/tws

Full length article

Experimental and numerical investigation of a rotational kirigami system

Isabel M. de Oliveira [a,*], Eduardo M. Sosa [b], Emily Baker [c], Sigrid Adriaenssens [a]

[a] Princeton University, Department of Civil and Environmental Engineering, Princeton, 08544, NJ, USA
[b] West Virginia University, Department of Mechanical and Aerospace Engineering, Morgantown, 26506, WV, USA
[c] University of Arkansas, Fay Jones School of Architecture and Design, Fayetteville, 72701, AR, USA

ARTICLE INFO

Keywords:
Deployment
Finite element analysis
Nonlinear buckling
Plastic hinge
Kirigami
Sheet metal

ABSTRACT

Engineered kirigami strategies enable structural systems that reduce cost and energy through flat-packing and rapid assembly. We studied the effect of the polygonal shape and cut pattern on the structural behavior of rotational kirigami units under tension and compression loads. Multi-step finite element models were developed, compared to experiments, and shown to predict experimental results robustly in the decimeter scale. We evaluate buckling-to-deployment load ratios, showing the load-carrying capacity of the system, and present a sensitivity analysis on localized geometric imperfections. These verified models can be used to further develop the system for load-carrying applications at larger scales.

1. Introduction

Kirigami, or the practice of applying patterned cuts to sheets of material, is being widely explored for engineering applications at various scales, from nano to meter [1–8]. Engineering applications include building-scale structural elements, facades, shading systems [1,7,9–13], solar tracking systems [14], damping systems for impact loads [15], haptic swatches [16], wearable electronics [17], soft robots [18], and many more [4]. Kirigami has also provided an open field for artistic exploration in sheet metal, taking advantage of the material's plasticity [6–8,19,20]. The fabrication of structures from planar sheets [21] is of interest to the construction industry for flat-packing, shipping material to construction sites, digital transmission of part files, and rapid deployment and assembly of structures. These features can reduce cost, construction material, time of assembly, and transportation resources [22].

In the centimeter and meter scales, two similar kirigami patterns present enhanced mechanical properties and fast deployable methods: the 'kirigami spin-valence' [7] and the 'rotational erection system' (RES) [23]. Cuts and folds are used in sheet material to generate polygonal RES units [23]. The linear hinged folds and hub rotations create out-of-plane extensibility and are instrumental in providing bistability to the system. The central development of RES has been in deploying individual collapsible units with bistability properties [24]. RES has been explored in surface form with units side by side acting independently from each other in their post-deployment load-carrying behavior [25]. The spin-valence kirigami system is similar to RES, using cuts and plastic hinges in sheet material [7] to provide out-of-plane extensibility. This system is stable during the deployment stage. The absence of bistable behavior in the spin-valence system allows selection of the deployment height without prior definitions. That is, the system does not snap to specific bistable configurations as the RES does. The main application of spin-valence kirigami has been in multi-unit systems where the vertices of adjacently deployed units connect to form a spatial structure.

While the systems are similar, RES has been primarily explored in centimeter-scale applications, and spin-valence has been predominantly explored in meter-scale applications. Another difference between the two systems is that spin-valence kirigami requires only cuts on sheet to produce the concentrated strains at hinge areas. By reducing the cross-section at specific locations, the hinges form during the deployment process. The RES, on the other hand, requires that fold lines be inserted along prescribed lines in addition to the cuts to guide where highest deformations will occur. The fabrication of fold lines would require an additional geometric definition for these lines and another manufacturing step when compared to the spin-valence system.

In the present work, we focus on introducing and reviewing relevant components of the spin-valence kirigami system for three main reasons: (1) previous studies of the system show its promise for structural applications [26]; (2) bistability is not a required property for load-carrying capacity; and (3) it is desirable to reduce a manufacturing step by avoiding fold lines. From this point forward, we will refer to this system more broadly as a rotational kirigami system, which can be in its single- or multi-unit configuration.

The differently shaded regions of Fig. 1 indicate the correspondence of the system components between flat and deployed states. Fig. 1(a)

* Corresponding author.
E-mail address: imdo@princeton.edu (I.M. de Oliveira).

https://doi.org/10.1016/j.tws.2023.111123
Received 4 April 2023; Received in revised form 7 August 2023; Accepted 14 August 2023
Available online 25 August 2023

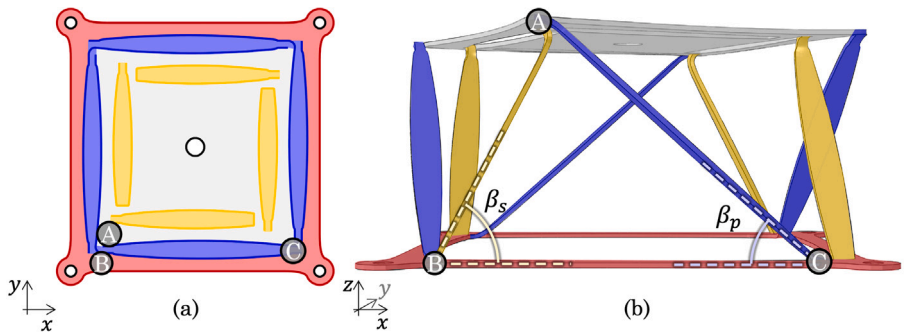

Fig. 1. Rotational kirigami (a) flat cut pattern and (b) deployed state with reference points in flat and deployed configurations. Points A, B and C produce triangulation in the deployed configuration. The primary leg $\overline{BC}$ forms angle β_p with the base $\overline{BC}$ and the secondary leg $\overline{AB}$ forms angle β_s with the base $\overline{BC}$.

shows the cut pattern of the rotational kirigami system. Fig. 1(b) shows the deployed state of this cut pattern. The deployed state produces triangulation formed by vertices A, B and C, providing structural stability to the system.

Planar space frame versions of the rotational kirigami system have been evaluated as appropriate for sculptural and facade applications [26], but design changes are required for structural applications. Plastic hinge formation at diagonal endpoints is central to the mechanical behavior of the system. Therefore, previous studies [26] indicated a need to study the hardening effect of the system to avoid brittle failures. In previous studies, this system presented increased strength due to contact between the frame diagonals; however, these interactions were unreliable [26]. It is suggested [26] to apply design changes to the diagonals to ensure contact occurs to increase the strength of the system reliably. Additionally, the system ductility is highly dependent on the unit configuration. Consequently, further study on the unit deployability and connectivity configurations should be conducted to enable a system with enhanced mechanical properties [26,27].

The rotational kirigami system can additionally be applied to doubly curved surfaces [9], exemplifying the possible extensions of the applications of this fabrication method. The cut pattern of irregular polygons and tessellation of the surface with different types of polygons pose many geometric and performance optimization challenges. Geometric challenges such as connecting the deployed vertices of adjacent units must be coupled to the highly constrained nature of the problem — the geometric cut pattern must not overlap itself for the fabrication to remain feasible from planar sheet material.

This rotational kirigami system shows promise in stiffening planar sheets through a straightforward fabrication method and efficient use of material. Nevertheless, the literature lacks – and calls for – a systematic study of material and geometric parameters of these patterns suitable for large-scale structural design applications [9,26,27].

The objective of the present work is to provide a detailed study of four designs of single-unit rotational kirigami systems to investigate their mechanical behavior during deployment and under compression. We strive to understand the behavior of single-unit systems to enable future parametric studies of single- and multi-unit systems – a topic out of the scope of the present work. This study includes single polygonal units ranging from triangles to hexagons at the decimeter scale and reports steps to manufacture the units to provide a consistent and replicable process. This study specifically focuses on four geometric designs to learn how reliably the system can be fabricated and how hinges are formed during the deployment process with the chosen material and geometry. Previous work provided information that the hinges form in concentrated areas [7,26,27]. However, due to limited information on previously used material and changes to the cutting patterns introduced in this study, a detailed investigation of the system mechanics becomes necessary to show this behavior holds. Once we show (1) the extent of hinge formation, (2) the possibility to reliably fabricate and test the system, and (3) a representative numerical simulation of the physical system, then we will extend the current study in future work to other types of models. This future work will include the objective of learning correlations between each of the system parameters. Extensive parametric studies of system components are beyond the scope of the present work. The chosen length scale for this study is designed to fit the available testing equipment size and tolerances and to enable qualitative comparison to previous work in the literature [7,26,27].

Table 1
Geometry of polygonal kirigami units: design dimensions.

N –	r_{bound} [mm]	w_o [mm]	w_w [mm]	w_{pinch} [mm]	ℓ_{pinch} [mm]	ℓ_p [mm]	ℓ_s [mm]	α [deg]
3	104	8	11[a]	5	8	129	66	0
4	127	9	13	5	8	147	104	0
5	95	6	9	5	8	94	74	15
6	104	5	9	5	8	91	81	26

[a]N3 secondary leg width $w_w = 9$ is different to primary leg width $w_w = 11$.

We organized the present work into five sections, as follows. We surveyed the literature in the present section (Section 1). We provide materials and methods required to generate the geometric cut pattern and finite element models and to fabricate and test specimens in Section 2. We compare and contrast the numerical models and experiments in Section 3, discussing those results and qualitatively comparing them to the work mentioned in Section 1. Section 4 outlines the future work required to overcome identified challenges, and Section 5 provides a summary of our findings, concluding the present work.

2. Materials and methods

2.1. Geometry of rotational kirigami units

The present work studies the effect of varying the polygonal shape of rotational kirigami units on the unit deployment and compression behavior. We investigated four regular polygonal shapes for numerical and experimental evaluations: a triangle ($N = 3$), a square ($N = 4$), a pentagon ($N = 5$), and a hexagon ($N = 6$). All shapes contained four essential components to generate a rotational unit cut pattern: a *boundary polygon*, an inner polygon or *hub*, a set of *primary legs* connecting the boundary polygon to the hub, and a set of *secondary legs* connecting the hub to the boundary polygon. These components are shown in Figs. 2(a) to 2(e).

In addition to the number of polygon sides N, Fig. 2 shows the following design parameters: r_{bound} boundary polygon radius; w_o offset width; w_w widest leg cross-sectional width at mid-span; w_{pinch} pinched area width; ℓ_{pinch} pinch length; ℓ_p primary leg length; ℓ_s secondary leg length; and α secondary leg in-plane angle of rotation. Table 1 shows the dimensions of each parameter.

The global (e.g., leg length ℓ_p or ℓ_s) and local (e.g., leg cross-sectional width w_w) geometric parameters heavily depend on one

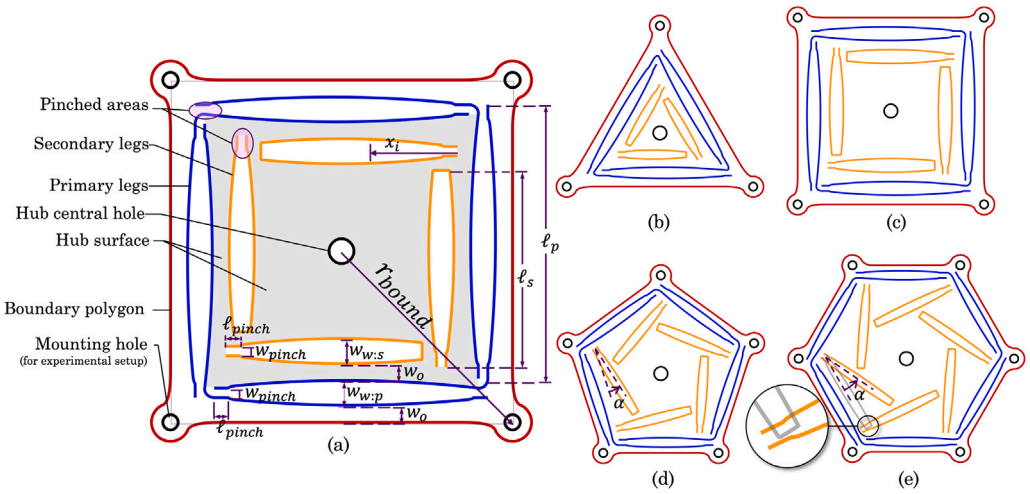

Fig. 2. Components and instances of polygonal cut patterns: (a) parameters involved in the creation of cut patterns; (b) triangle; (c) square; (d) pentagon; and (e) hexagon. Detailed call-out in (e) shows the resulting overlapping geometry if secondary legs were not rotated.

another. For a fixed boundary polygon radius r_{bound}, all remaining parameters must fit within that boundary such that no component overlaps another. This constraint is due to the fabrication of the system from single sheets of material. The primary legs centerlines have a polygon radius R_p from Eq. (1). The secondary legs centerlines have a polygon radius R_s from Eq. (2). Therefore, each defined width reduces the maximum possible length for the components nested in that geometry. For example, if the offset is first determined in a square unit, the maximum value for primary leg lengths is reduced by twice that amount, and the secondary leg lengths are reduced by four times that amount.

$$R_p = r_{bound} - \frac{w_o + \frac{w_w - w_{pinch}}{2} + \frac{w_{pinch}}{2}}{\cos\frac{\pi}{N}} \tag{1}$$

$$R_s = R_p - \frac{w_o + (w_w - w_{pinch}) + w_{pinch}}{\cos\frac{\pi}{N}} \tag{2}$$

The polygon geometries have the same pinch length ℓ_{pinch} and width w_{pinch} (Fig. 2(e)) for both primary and secondary legs across all polygons. For comparison purposes, all polygons would ideally have the same leg length and angle between the legs and the boundary polygon (i.e., β_p and β_s in Fig. 1) or the same polygonal radius r_{bound}. However, the primary leg lengths and polygonal radii differ slightly among units due to the experimental setup limitations, such as the available physical space in the testing apparatus and practical fabrication of the mounting plate. Therefore, three design ratios were specified to be similar among different polygons to provide an initial design guide to define the unit's dimensions: primary leg length to leg width ratio, ℓ_p/w_w; secondary leg length to width ratio ℓ_s/w_w; and polygon side length to offset ratio ℓ_{bound}/w_o. These ratios provide in-plane geometric similarity among different legs and units, but they do not produce similarities for out-of-plane mechanical properties which heavily rely on the thickness of the sheet [28]. The use of these ratios is simply to induce selection of higher cross-sectional areas while limiting the reduction of the leg length, providing a means for initial selection of the geometry dimensions. Table 2 summarizes the resulting geometric ratios according to geometric nesting design considerations. The lower the design ratio, the less each component is prone to local buckling, even if marginally, due to increased cross sectional area.

When deployed, the final geometry produces a triangulated system (see Fig. 1). In this system, the larger the difference between primary and secondary leg lengths, the more uneven is the triangulation between the legs and the base for a vertical compression load [29]. The more uneven the triangulation is, the more the loads get concentrated in one leg instead of being distributed among both legs [30]. Given this interplay between lengths, widths, and change in the deployed unit triangulation, we chose to rely on simplified design ratios to provide an initial guide into choosing these dimensions. Here, we focused on uncovering the extent of plastic hinges, defining a reliable numerical model for a given design and material, and identifying the system's parameters to be examined in future parametric studies. Hence, understanding the correlation between each of these geometric properties and the mechanics of the system is beyond the scope of the present work.

Table 2
Geometry of polygonal kirigami units: design ratios for initial selection of system dimensions.

N	ℓ_s/w_w	ℓ_p/w_w	ℓ_{bound}/w_o
3	8.0	12.0	17.0
4	11.0	11.0	17.0
5	10.5	10.5	17.0
6	10.6	10.6	17.0

Within the geometric constraints (i.e., avoid overlapping components, see call-out detail in Fig. 2(e)), the secondary legs in the pentagon and hexagon units can be longer than the polygonal edge length when rotated. These legs reached the target design ratios when rotated by an angle α defined through observation during geometry generation (see Figs. 2(d), 2(e) and Table 1). This increase in leg length due to rotation is not achievable in the triangular and square polygons due to intrinsic geometric properties. That is, the more the secondary legs rotate in triangles and squares, the smaller the maximum possible leg length is. This property can be drawn from observing the design space of regular polygonal units ranging from triangles to hexagons. Once the geometric characteristics of the cut pattern were defined, each line was given a thickness defined by the cutting tool (see Section 2.3). Corner and central holes were included for testing mounting purposes.

2.2. Numerical analysis

Based on the cut pattern outline, a surface was generated using Rhinoceros3D/Grasshopper3D [31] for numerical modeling. This surface was then imported into Simulia/Abaqus [32] to create a finite element (FE) model. The main features of the multi-step FE models generated for each polygonal shape are described as follows.

Parts and elements. The model consists of one part generated from the geometry imported from Rhinoceros3D [31] and is defined as a single surface with holes and cuts. We selected shell elements to provide

an FE model closest to the physical problem, where two dimensions are larger than the third at a reasonable modeling cost. The reasons behind the implementation of this type of modeling included three main considerations:

- *Geometric considerations.* Since the base geometry must be fabricated from a single thin flat sheet, a model constituted by shell elements with the thickness of the flat sheet would be sufficient to represent the behavior of the units in every stage of the modeling process — from the definition of the initial cut pattern to the final deployed and deformed shape.
- *Fabrication considerations.* A model with these types of elements can capture mechanical responses due to the cut tool width (see Section 2.3), a feature difficult to capture with bar and hinge models. This feature is inherent in the steel sheet fabrication process, and it changes the mechanical response of the system by reducing the cross-sectional width.
- *Computational time.* Since the computational time is proportional to the mesh density, a model based on shell elements would provide acceptable results at a reasonable computational cost compared with a model based on solid elements. A model with solid elements would require higher mesh density, including more than one layer of elements across the sheet thickness, to avoid shear-locking behavior [32].

This single surface was discretized with a combination of linear triangular (S3) and quadrilateral (S4) shell elements, with mesh refinement in the pinched areas (see Section 3.1) The combination of triangular and square elements produced a better mesh fitting in areas with a small radius of curvature and reduced the distortion of quadrilateral elements due to tight curvatures. The part was given a constant sheet thickness of $t = 1.89$ mm to model a sheet with gauge 14.

Interactions and boundary conditions. The model includes two sets of connector elements (CONN3D2): axial and weld connectors. These connector elements were used for a point-to-point connection between two parts of the mesh. Fig. 3 shows these elements for the case of a square unit. Both types of elements are defined at the initial model set up Fig. 3(a), but they are only activated in specific steps of the analysis as detailed in the analysis steps below. The axial connectors link the base of the boundary polygon to the free end of the secondary legs located in the hub surface. We used the axial connector elements to apply a prescribed displacement to join the free end of the secondary legs with their corresponding base point. Each secondary leg has one axial connector. The axial elements have no mechanical behavior associated to them; they only track the length between the two points they connect throughout the analysis. The weld connectors were implemented in groups of four elements per leg, connecting four points of the free end of the secondary leg with four points at the base of the boundary polygon. For example, a triangle unit has twelve weld and three axial connectors. The same connector configuration was implemented for all polygonal units. The weld connector elements are only activated once the free ends of the secondary legs reach the corresponding position at the base. At this stage, contact interactions were not included in the models. Self-intersection was avoided by visual inspection of each model step result. Bolted corners were modeled as fixed translations at the mounting hole edges. This boundary condition is propagated for all the analysis steps (shown in Fig. 5).

Material properties. Carbon steel was selected due to its known malleability and strength from work shown in the literature [7,26,27]. Steel type CS A1008 exhibits similar material properties to those in precedent rotational kirigami units [26]. Material properties obtained from a material atlas [33] provided an initial stress–strain curve for A1008 steel for the FE models. These initial models predicted the range of expected buckling loads and aided the geometric design of kirigami units to comply with testing machine constraints. Uniaxial tensile tests were conducted with standard dogbone specimens cut from the A1008 steel sheet used in the experiments to confirm the assumed material properties (see Section 2.3). The engineering stress–strain relationship obtained from the material testing is shown in Figs. 4(a); 4(b) compares the plastic region obtained from the material atlas [33] with the curve obtained from the material testing. After conducting these tests, we updated the models to include the properties of the material used in the experiments. Section 3 presents result analyses using the yielding stress value of $\sigma_Y = 186$ MPa. Elastic material properties are defined by $E = 200$ GPa and $\nu = 0.3$. Plastic material properties are defined with isotropic hardening, and in tabular form using true stress and true strain values obtained from the curve in Fig. 4(b). The elastic properties, the yielding strength σ_Y, and a tabular form of the curve in the plastic region are the parameters that defined the material constitutive model implemented in Abaqus [32].

Analysis. The final three-dimensional geometry of the deployed hub was reached through a geometrically nonlinear quasi-static six-step sequential analysis implemented in Abaqus/Standard [32]. The first five steps are static general steps for stress analysis, and the sixth is a static Riks step [32] to simulate the nonlinear buckling behavior of the compressed unit. This sequential analysis carries all internal stresses from step to step and is depicted in Fig. 5. The different steps are:

Step 1. **Hub deployment.** A prescribed vertical displacement on the hub center hole deploys the hub (Fig. 5(a)). The magnitude of the prescribed displacement depended on the polygonal shape: 70 mm for N3; 110 mm for N4; 76 mm for N5; and 80 mm for N6. We defined these heights to provide room for secondary leg deployment and avoid any intersection with other unit parts.

Step 2. **Hub release.** The prescribed displacement used for lifting the hub center hole is deactivated (Fig. 5(b)). The hub is allowed to move downwards until it reaches a new equilibrium position.

Step 3. **Secondary leg deployment.** A concentrated rotation is applied to each of the secondary legs for initial deployment. The concentrated rotation is applied within the pinched area of the leg at $4t$ distance from the hub surface, where t is the sheet thickness, to deploy the legs downwards to form a 90° angle with the hub surface. During the secondary leg deployment, the hub surface is kept in place with fully fixed boundary conditions (Fig. 5(c)).

Step 4. **Secondary leg deployment with a connector element.** The axial connector elements are activated to join the free end of the secondary legs to the designated welding line on the boundary polygon base. Axial elements were defined in the initial model set up, and have a reference length equal to the distance between the two points it connects (d_0) (see red lines in Fig. 3(a)) [32]. To deploy the secondary leg, the axial element is used to prescribe a displacement equal to negative of the reference length ($-d_0$) therefore, joining the two points of the mesh that it connects together (see Fig. 3(b)). The fixed hub surface is released for this step as the hub height changes to connect those points. The weld connector elements are shown in Fig. 3(b) only as reference, but they are not activated in this step.

Step 5. **Welding of secondary legs.** The weld connector elements are activated. The weld connector element fixes the translation and rotation between points on the free end of the secondary legs and the boundary polygon base, creating continuity between both parts of the mesh (Figs. 3(c) and 5(d)–(e)).

Step 6. **Nonlinear buckling analysis.** In the final step, a prescribed displacement is applied on the entire hub surface to compress the unit (see Fig. 5(f)). Two scenarios were considered in this step to simulate the presence of the compression plate. The first one allowed the in-plane rotation of the hub as the unit was compressed, and the other one locked the rotation of the hub as it moved downwards in the z axis. The boundary polygon surface was restricted to move on the vertical axis (z axis) to simulate the base plate (Fig. 5(f)). The weld connector elements remain activated.

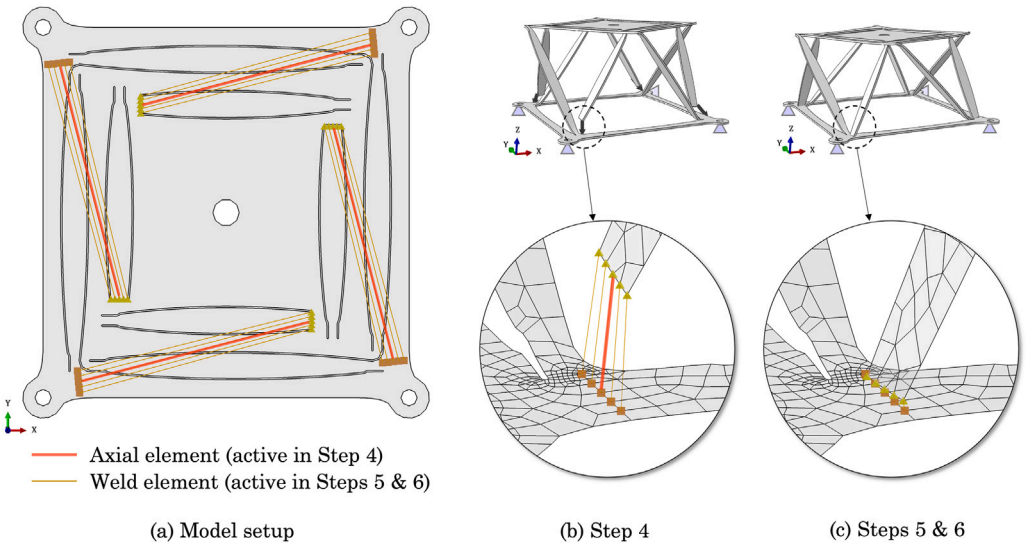

Fig. 3. Connector elements are defined during the (a) initial model setup, shown here for the case of a square unit. The axial elements (b) are activated in Step 4 of the analysis, while the weld elements (c) are activated in Steps 5 and 6. Analysis steps are described in Section 2.2 and in Fig. 5. The zoomed call-outs (b) and (c) show the mesh used for a square unit, showing which points of the mesh each of the connecting points are attached to. The full mesh for one unit and discretization studies are shown in Section 3.1 and Fig. 9.

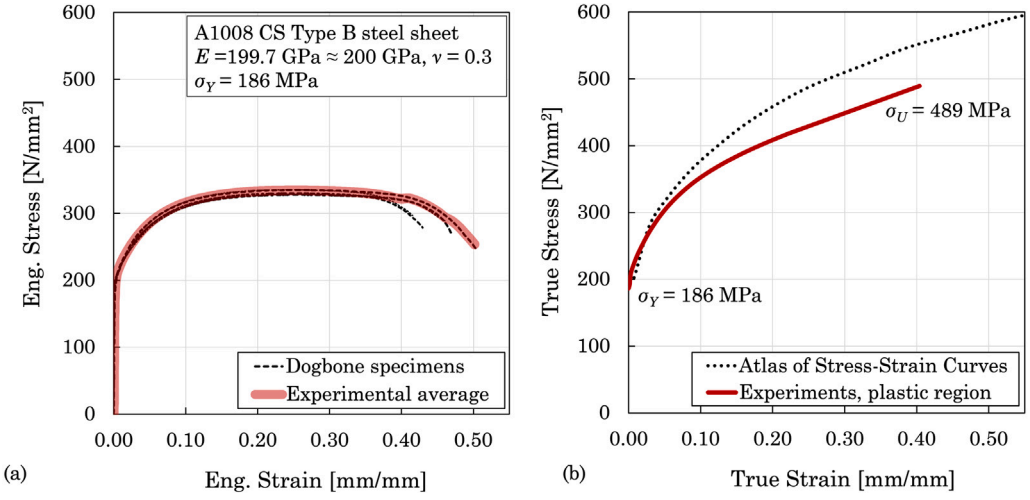

Fig. 4. Material properties: (a) Experimental engineering stress–strain curves for CS A1008;(b) True stress–strain relationships for plastic region obtained from [33] and material testing conducted in this study.

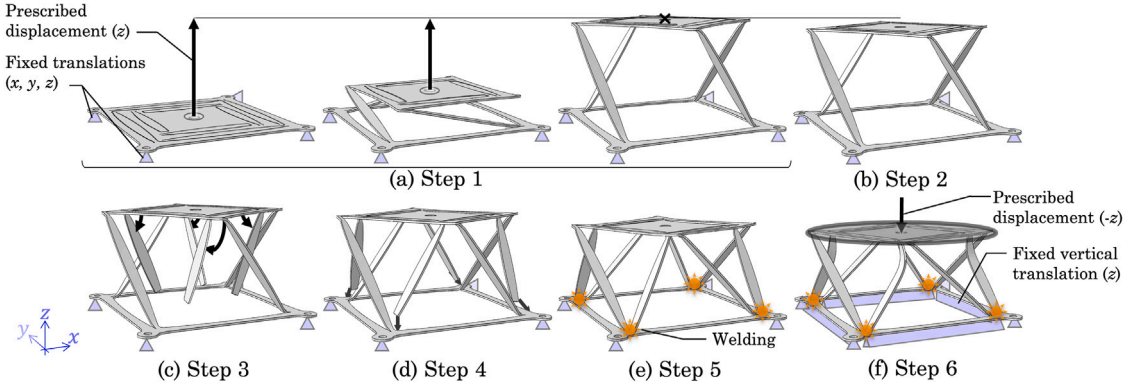

Fig. 5. Sequence of six consecutive analysis steps implemented in the FE model for a square unit (N4) and repeated for all the other polygonal shapes: (a) Step 1: hub deployment with prescribed displacement; (b) Step 2: hub release; (c) Step 3: secondary leg deployment with a prescribed rotation; (d) Step 4: secondary leg deployment with a prescribed displacement; (e) Step 5: welding of the secondary legs to the boundary polygon; (f) Step 6: nonlinear buckling analysis with a prescribed displacement and fixed vertical displacements on boundary polygon base.

Sets of FE models. The FE analyses included three sets of models: free hub rotations for all units, fixed hub rotations for all units, and secondary leg bending curvature study. The free and fixed hub rotations models were created to show the effect of decoupling the hub vertical displacement and rotation about the vertical axis on the buckling load. The secondary leg bending curvature study is a set of parametric analyses conducted to understand the effect of this curvature on the buckling load of square units under free and fixed hub rotation boundary conditions. Section 3 shows two different secondary leg curvature studies, and the square was selected as a representative unit for a detailed curvature sensitivity study.

2.3. Experimental setup

The rotational kirigami designs described in Sections 2.1 and 2.2 were manufactured and tested according to the following sequence.

Cutting. The polygonal shapes were cut from a single flat A1008 carbon steel sheet, gauge 14 (1.897 mm nominal thickness), using a waterjet cutting machine (Intec-G2-510, Techni, Charlotte, NC) at a cutting speed of 10 m/min as shown in Fig. 6(a). The thickness of the cutting nozzle was 0.75 mm. Five units of each polygonal shape were cut for subsequent testing. Standard dogbone specimens were also cut from the steel sheet for material characterization under tensile loading following the ASTM E8-22 standard.

Hub deployment. A customized testing fixture was created to mount the flat kirigami units and produce initial hub deployment by tensile loading. The fixture consisted of a 300 by 200 mm base steel plate. This base plate was mounted in a tabletop universal testing machine (Shimadzu, Kyoto, Japan) with 5 kN and 10 kN load cells. The flat kirigami units were mounted on the base plate, aligned and bolted at the corners of the polygonal shapes, shown in Fig. 6(b). To ensure a consistent force distribution, a torque of 5 Nm uniformly tightened all the bolts, shown in Fig. 6(c). For initial deployment, an eyebolt and steel shackle connected the hub center to a swivel hoist ring, all rated for lifting, shown in Fig. 6(c)–(d). The swivel hoist ring allowed in-plane hub rotation during its initial deployment. The hubs of the polygonal units were deployed by the automated lifting of the testing machine crosshead at a rate of 10 mm/min, shown in Fig. 6(d). Once the initial deployment was completed, the hub was released by a downward 10-mm displacement of the machine crosshead, and then the entire kirigami unit was removed from the mounting plate. The force necessary to lift the hub connected to the primary legs was recorded and compared to the FE simulation results later. All hubs were deployed with counterclockwise rotation except for an additional square unit deployed clockwise.

Secondary leg deployment. A customized bending tool comprised of a clamping mechanism and a lever arm was created for the initial deployment of the secondary legs of each polygonal unit. This bending tool was designed to produce a consistent, concentrated rotation at the location of the pinched areas of the secondary legs. The bending tool was clamped to the already deployed hub. The levering arm was used to apply a concentrated bending force to produce an initial downwards 90° rotation to each of the secondary legs, as shown in Fig. 6(e).

Secondary leg final placement. After the initial rotation, the bending tool was left connected to the hub to guide the curvature of the secondary legs, as shown in Fig. 6(f). Then, the free ends of the secondary legs were manually driven to the pinched areas of the primary legs connected to the base hub. This step completed the deployment of the secondary legs. The final position of deployed secondary legs is shown in Fig. 6(g).

Welding of secondary legs. The free ends of the secondary legs were joined to the boundary polygon base by tungsten inert gas (TIG) welding with a single-sided fillet weld. The weld length was equal to the width of the secondary leg free end (6 mm). During the welding process, a weight was added to the hub to ensure that the free ends of the secondary legs were in contact with the base surface as shown in Fig. 6(h).

Compression testing. The sets of five specimens per polygon fabricated were divided into three sets. Set 1 comprised of three specimens for each polygonal unit manufactured as described in the present section. Set 2 included two specimens of each polygonal unit that were modified. The secondary legs of Set 2 were locally formed with a hammer to produce smaller bending curvature between the secondary legs and the hub surface. An additional square unit composes Set 3. This unique specimen was fabricated exactly like Set 2, except for its deployment in the opposite direction as the other units, using a clockwise motion. This additional specimen allowed the realization of a compression test with fixed hub boundary conditions. Due to the availability of testing specimens, we were limited to one specimen for the N4 category to perform a fixed hub boundary condition test. The relatively small variability observed in the results of experimental Sets 1 and 2 shown in Section 3.2 provided confidence that a single specimen would be sufficient to capture the change of loading-carrying capacity with a change in the hub boundary condition. The resulting three-dimensional kirigami units of Set 1 and Set 2 were mounted on the same base plate used for initial deployment and subjected to uniform compression. Like in the initial deployment, the corners of the polygons were bolted to the base plate with a uniform torque of 5 Nm. A 200-mm diameter and 19-mm thick steel plate connected to the machine crosshead and load cell compressed the units at a displacement rate of 1.5 mm/min until reaching a downward displacement of 25 mm, as shown in Fig. 6(i). The compression load was recorded and used for comparison with the FE simulation results.

3. Results and discussion

Results are presented in two sections. First, different aspects of the initial deployment by tensile loading are presented, followed by a description of the compression behavior of the deployed kirigami units. Each section discusses various aspects of the experimental results and compares them with their corresponding FE simulation results.

3.1. Initial deployment

In Section 2.3, the tensile testing methods of 3- to 6-sided polygonal kirigami specimens were described for the initial deployment tests. Figs. 7(a) and 7(b) show side views of the initial deployment sequence by tensile loading corresponding to shapes N4 and N6, respectively, as an example. The sequence of deployment predicted by the FE simulations agrees with the experimental results for all polygonal shapes. Results in Fig. 7 show that as the hub area was lifted from the central attachment point, the endpoints of the primary legs connecting the upper hub to the lower base polygon gradually bent. In this process, the legs simultaneously changed their position as the hub rotated around the vertical axis (z). We include a video comparing experimental and numerical results for the deployment of one N6 unit in the supplemental materials. Figs. 8(a) and 8(b) show the initial and rotated position of the hubs of the experimental testing specimens at the end of the initial deployment. For comparison, Figs. 8(c) and 8(d) show contours of vertical displacements (U3) and rotations around the z-axis (UR3) predicted by the FE models. Simulation results show that for the preselected lifting distances (summarized in Table 3), the hubs underwent a uniform rotation with values that reached maximum values ranging from 28° (N3) to 36° (N4). In comparison, N5 and N6 hubs rotated 32° and 30°, respectively. These values agreed with

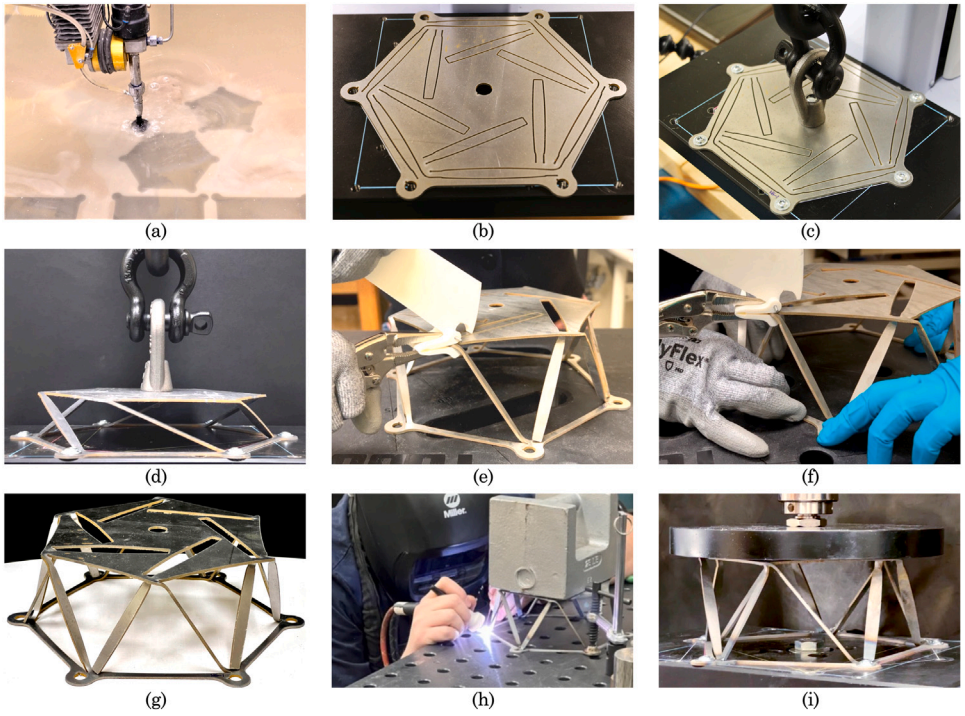

Fig. 6. Manufacturing and testing sequence: (a) Waterjet cutting; (b) Mounting and alignment on the base plate; (c) Bolting and preparation for initial deployment; (d) Hub deployment by tensile loading; (e) Initial secondary leg deployment by concentrated rotation; (f) Connection of secondary legs to base polygon; (g) Final leg position prior to welding; (h) Welding of secondary legs; (i) Compression test.

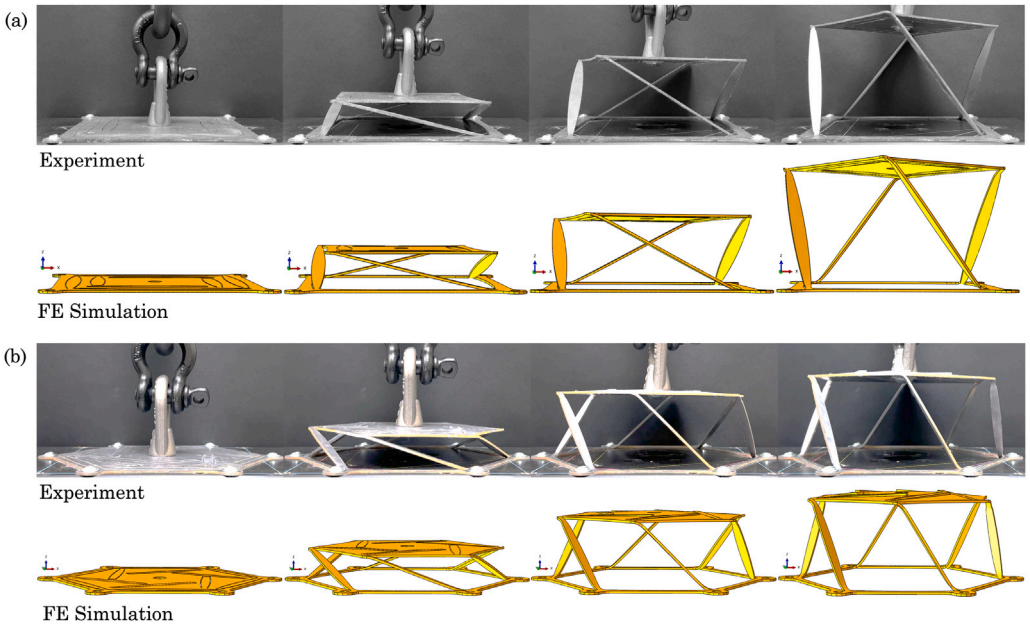

Fig. 7. Side view of the sequence of initial deployment: (a) N4 specimen; (b) N6 specimen.

those captured experimentally (see Table 3). The experimental hub rotations were measured from video stills captured during the initial deployment. During the tests, the video camera was located in an overhead position with respect to the test specimen pointing down and with an angle nearly perpendicular to the hub surface. The testing setup and specimens included pre-drawn lines as references for the initial and final position after the hub rotation. The resulting images were then imported into an image post-processor, which included a digital protractor that used the reference lines to measure the resulting rotation angles.

Fig. 9(a) shows the experimental forces necessary to lift the hub of all polygonal shapes as part of the initial deployment. The variation of force–displacement trajectories displays two distinctive stages as the hub moves upwards. First, a linear region for small vertical displacements is followed by a second region with a nonlinear trajectory until the specified lifting distance is reached. For all the polygonal shapes, the linear portion corresponds to the elastic behavior of the material in which the lifting distance is about 1 to 1.5 times the plate's thickness (t = 1.89 mm), as shown in the detail of Fig. 9(b). As the lifting force increases, the material enters the plastic region, forming plastic

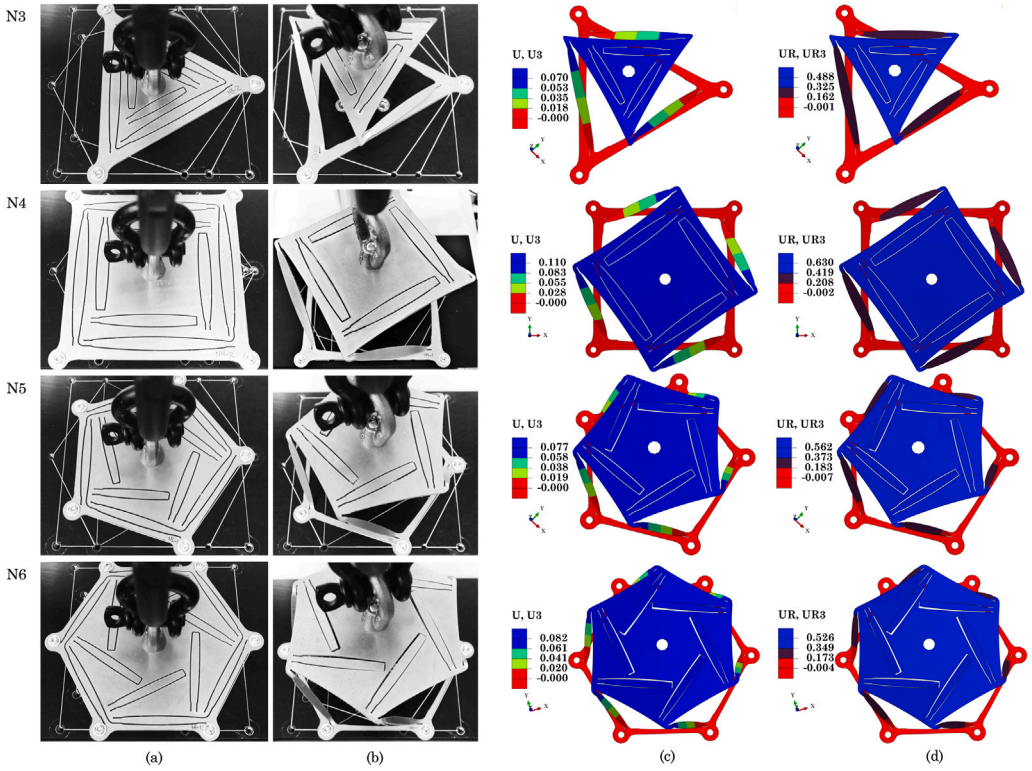

Fig. 8. Hub initial deployment and rotation, experiments vs. simulations: (a) Initial position; (b) Hub position after reaching target lifting distance; (c) Contour of vertical displacements (U3); (d) Contour of rotations around the vertical axis (UR3). Lifting distances and rotations are summarized in Table 3.

Table 3
Summary of hub elevations and rotations.

N	Lifting distance	Hub rotation after lifting			Height after release	Height after welding
	Exp. & FE [mm]	Avg. Exp. [deg]	FE [rad]	[deg]	Avg. Exp. [mm]	Avg. Exp. [mm]
3	70	27	0.488	28	68	63
4	110	35	0.630	36	105	96
5	75	31	0.562	32	72	71
6	80	29	0.526	30	78	76

hinges. This result shows that irreversible changes occur early in the unit deployment phase.

This behavior is expected as the hub deployment requires bending the primary legs endpoints to reach the specified lifting distance. These hinges behave elastically while the vertical displacements are within the order of magnitude of the plate thickness t. For hub displacements higher than t, the hinges transition to a fully plastic behavior characterized by larger deformations and increasing lifting forces as the steel hardens.

The lifting load–displacement trajectory of Fig. 9 matches the bilinear behavior obtained in [27] for quadrilateral units. The order of magnitude of the lifting forces in the present work agrees with those presented in the literature [27]. These similarities show the system has consistent deployment behavior regardless of manufacturing techniques. However, the system cannot be quantitatively compared due to differences in material properties, cut pattern specifications, cutting method, and sheet thickness.

Experimental results showed that the force required to deploy the hub increased as the number of primary legs connected to the hub increased. First, the forces to transition from the elastic to the plastic region were about 30 N (N3), 40 N (N4), 80 N (N5), and 100 N (N6) (see Fig. 9(b)). The forces necessary to reach the final deployed position were 110 N (N3), 150 N (N4), 300 N (N5), and 375 N (N6) (see Fig. 9(a)). Overall, the forces required to deploy N5 and N6 polygons resulted in about twice the forces required to deploy N3 and N4 polygons.

Furthermore, Fig. 9 shows that the force–displacement trajectories predicted by the FE models compared to the curves obtained experimentally. The experimental and simulation curves are practically coincident in the linear region, as shown in Fig. 9(b). In contrast, in the nonlinear area, the simulation curves tended to slightly overestimate the lifting forces for the same level of vertical displacement. A mesh sensitivity analysis was conducted using polygon N3 as a test case to examine the prediction accuracy of the simulation models. Figs. 9(d) and 9(e) show examples of two mesh densities considered for the analyses and the mesh densification at the location of the plastic hinges. Results summarized in Fig. 9(c) showed that initial simulations with a relatively coarse mesh with reduced integration shell elements (S4R and S3R) and element sizes in the order of $2t$ (labeled D4 and comprised of about 1,800 elements) provided deployment force results at a relatively low computational cost ($<$ 1 min). However, further simulation runs indicated that the force overprediction in the nonlinear region was related to the mesh density and shell element type selected for the models. Additional simulation results were obtained with denser meshes, in the order of $(1/2)t$ and $(1/4)t$ (labeled as D4, D1 and D05 and comprised of approximately 1,800 elements, 17,000, and 65,000 elements, respectively) of fully integrated elements (S4 and S3). These elements are better suited to capture the geometric nonlinear behavior originated by the large strains developed by the plastic behavior of

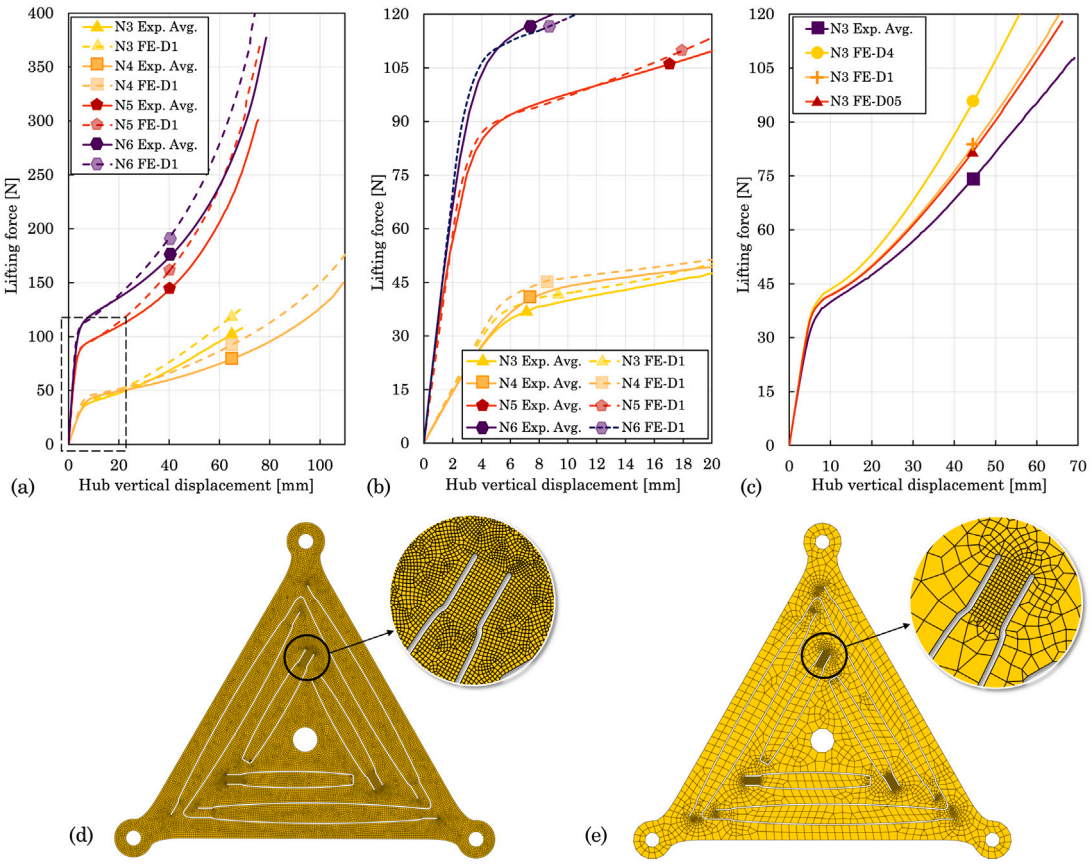

Fig. 9. Lifting force vs. vertical hub displacement. (a) Experiments vs. simulations for all polygonal shapes; (b) Linear region for all polygonal shapes; (c) Mesh density results for N3; (d) D05 mesh; and (e) D1 adaptive mesh used for all numerical analyses.

the steel plate [32]. Simulation results indicated that mesh density D1 improved the force prediction at a reasonable computational cost (≃ 10 min) with respect to mesh density D4. In contrast, mesh density D05 did not improve the results predicted by D1. Thus, mesh density D1 was implemented for computing the force–displacement curves of the other polygonal shapes shown in Figs. 9(b) and 9(c).

FE simulations were used to analyze the stress distribution at the end of the initial deployment. The magnitude of the von Mises stress indicated the level of stresses at the different regions of the kirigami units, as shown in Fig. 10(a). A closer look at the stress distribution indicates that, as expected and for all the polygonal shapes, the regions reaching or exceeding the yield strength are located between the endpoints of the primary legs and the vertices of the base polygons and the hubs. In these areas, the steel plasticity is fully reached and leads to the formation of plastic hinges. These hinges provide stable deformed states allowing the construction of the 3-dimensional shapes. On the other hand, the von Mises stress distribution shows that the undeployed secondary legs of all polygonal shapes are subjected to nearly zero stresses. For polygons N3 and N4, the plastic regions in the primary legs only extend to the regions closer to the joints. In contrast, in polygons N5 and N6, nearly the entire length of the primary legs have reached plasticity. This behavior is shown in Fig. 10(b), which shows the areas actively yielding on each polygonal shape. Fig. 10(b) also indicates that the central area of polygons N5 and N6, where the pulling force was applied, and at the corners of the polygon created by the secondary legs, have also reached plasticity. This behavior is not seen in polygons N3 and N4. This different stress distribution is attributed to the increased force necessary to deploy additional legs of N5 and N6 and to the formation of additional plastic hinges with the consequent hardening of primary legs resulting in other deformations of the hub. N3 to N6 specimens were manufactured with the same sheet thickness, and same pinched area dimensions, and only two factors significantly changed: number of legs and absolute length of legs. First, more legs signify more pinched areas (higher total cross-sectional area) to deform into hinges. More legs are also correlated to reducing the absolute length of legs with the designs provided herein, and smaller leaver arms require higher forces to deform the hinges near the base.

This behavior was also seen in the experimental tests in which the pentagons and hexagons presented a slightly dome-shaped surface. The highest point was the load application area in the hub center hole. N5 and N6 geometric specifications also generate steeper angles between primary legs and boundary polygon edges. Therefore, there is a change in hinge bending to axial tensioning of the legs. The square showed the least amount of hub deformations, almost imperceptible to the human eye. The triangle presented slightly uplifted pinched areas at the endpoints of the primary legs, shown in Fig. 10(c).

3.2. Compression of kirigami units

This section presents experimental and FE simulation results of kirigami units subjected to compression loading. Measurements from experiments are compared and contrasted to data collected from FE simulations. Such measurements and data include equilibrium paths and buckling loads, effects of change in hub boundary conditions on buckling loads, buckling modes, stress analyses and imperfection sensitivity analyses.

3.2.1. Equilibrium paths and buckling loads

Figs. 11(a) to 11(d) show the average equilibrium paths obtained from experimental Sets 1 and 2 for N3, N5 and N6 units, and Sets 1 to 3 for N4 units. Section 2.3 presented details on the characteristics of each set of specimens utilized for compression tests. As described in

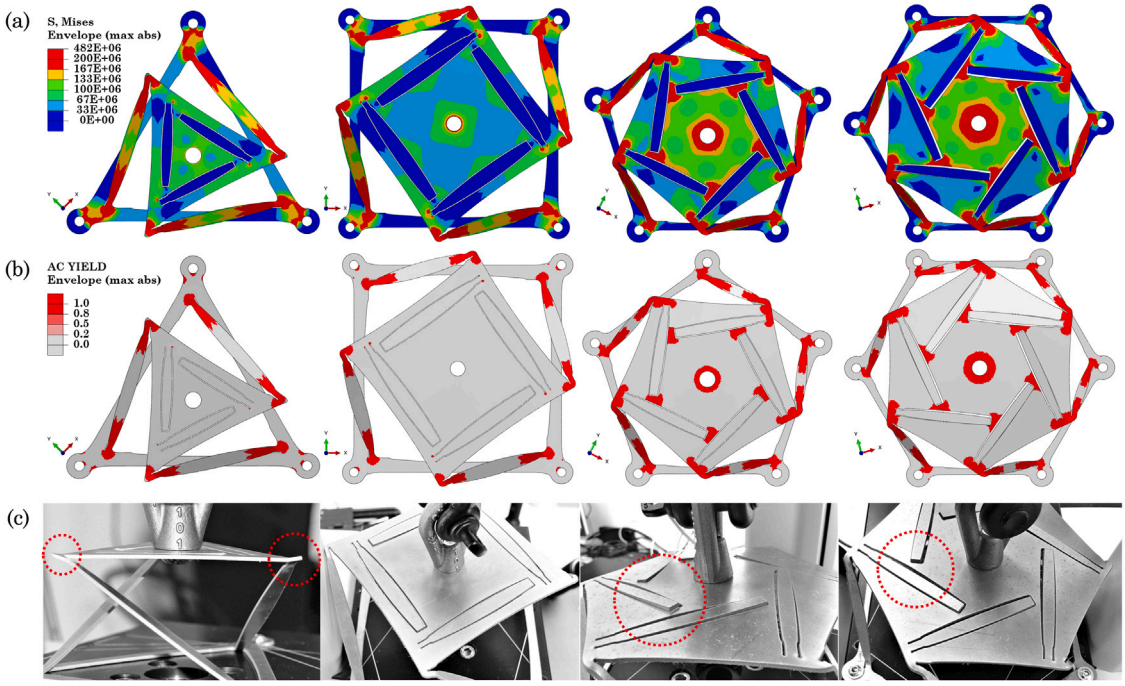

Fig. 10. Stresses predicted by simulations: (a) von Mises stress contours; (b) Contour of regions actively yielding (von Mises stress > 186 MPa); (c) Hub deformations at the end of initial experimental deployment.

Section 3.1, the polygonal hub surfaces were slightly deformed upwards at the end of the initial deployment and manufacturing process. Therefore, the initial compression load path presented a low-slope portion associated with the initial conformity of the kirigami specimen to the testing machine compression surface. Results presented in Figs. 11(a) to 11(d) show post-processed data averaged between units of each set, with excluded initial displacements due to the flattening of the hub. For each one of these equilibrium paths shown in Figs. 11(a) to 11(d), the shaded areas represent the range of standard deviation obtained from each set. The narrowness of the shaded areas indicate the consistency and low variability obtained from the experiments. The coefficient of variation (COV = Standard Deviation/Mean) at the peak compression load ranged from a 1% to 4% for all the sets, except for N6, Set 2, which resulted with a COV of 13%.

All the load–displacement curves shown in Figs. 11(a) to 11(d) are characterized by a primary pre-buckling equilibrium path and a secondary post-buckling path. The pre-buckling path follows a nearly linear trajectory corresponding to the elastic deformation of the material due to the compression load. The post-buckling path follows an unstable nonlinear behavior in which, after reaching the maximum compression load, the legs of the kirigami unit are deformed and cannot carry more load as the deformation increases. The unit's geometric imperfections inherent to the manufacturing process can explain part of the slight difference in slopes of the pre-buckling paths of Set 1 and Set 2, as well as the nonlinearity surrounding the maximum load and the post-buckling behavior. We refrain from providing further possible explanations of this change in slope due to the complexity of the system, and focus on the resulting peak loads that are well predicted by the FE model. The equilibrium paths of the polygonal kirigami units follow a behavior similar to cylindrical shells, particularly those subjected to uniform axial compression [34,35] and of isotropic material, pressure-loaded spherical shells [36], beam–columns, and some two-bar frames [34]. These systems are imperfection-sensitive systems and are subject to sudden buckling under static loading. The instability of these structural configurations is due to material and geometric nonlinearities [34,37]. The behavior of these paths matches the behavior of experimental results reported in [27].

Experimental results of Figs. 11(a) to 11(d) show average buckling loads ranging from 1,668 N for N3 units to 5,184 N for N6 units. The buckling loads increased as the number of polygonal sides and their corresponding pair of triangulated legs increased. This increase in compression capacity is expected as additional pairs of legs contribute to carrying additional compression load. Figs. 11(a) to 11(d) show a clear increase in buckling load for polygons with more edges and thus more legs.

A closer look at the experimental Sets 1 and 2 in Figs. 11(a) to 11(d) indicates that Set 2 units presented higher buckling loads when compared to Set 1 for all polygonal shapes. The increase in buckling load between the two sets is associated with the reduction of the radius of curvature in the transition between the secondary legs and the hub surface of Set 2. This reduction in the bending radius of curvature can be seen as a reduction of the geometric imperfection resulting from the bending process applied to deploy the secondary legs during manufacturing.

The percentage of buckling load increase between Set 2 and Set 1, summarized in the first row of Table 4, indicates that the increases differ among polygonal shapes. A plausible reason for the non-uniform load increase between different polygonal units is related to the different primary to secondary leg length ratios (ℓ_p/ℓ_s) of each unit. In this kirigami system, the larger the difference between primary and secondary leg lengths ($\ell_p/\ell_s \gg 1$), the more uneven is the triangulation between the legs and the base. This factor influences the load distribution among primary and secondary legs for a fixed vertical compression load [29,30]. While this ratio can be one of the reasons for non-uniform load increase, there are other reasons to consider, such as different slenderness ratios of legs of different polygonal units [38]. In-depth analyses of these factors fall beyond the scope of the present work and are here identified to be considered for future parametric studies on the geometry of the units.

3.2.2. *Effect of hub boundary conditions on the buckling load*

Figs. 11(e) and 11(f) compare the average equilibrium paths obtained experimentally with the equilibrium paths predicted by the FE models. Two hub boundary conditions shown in Figs. 11(e) and 11(f)

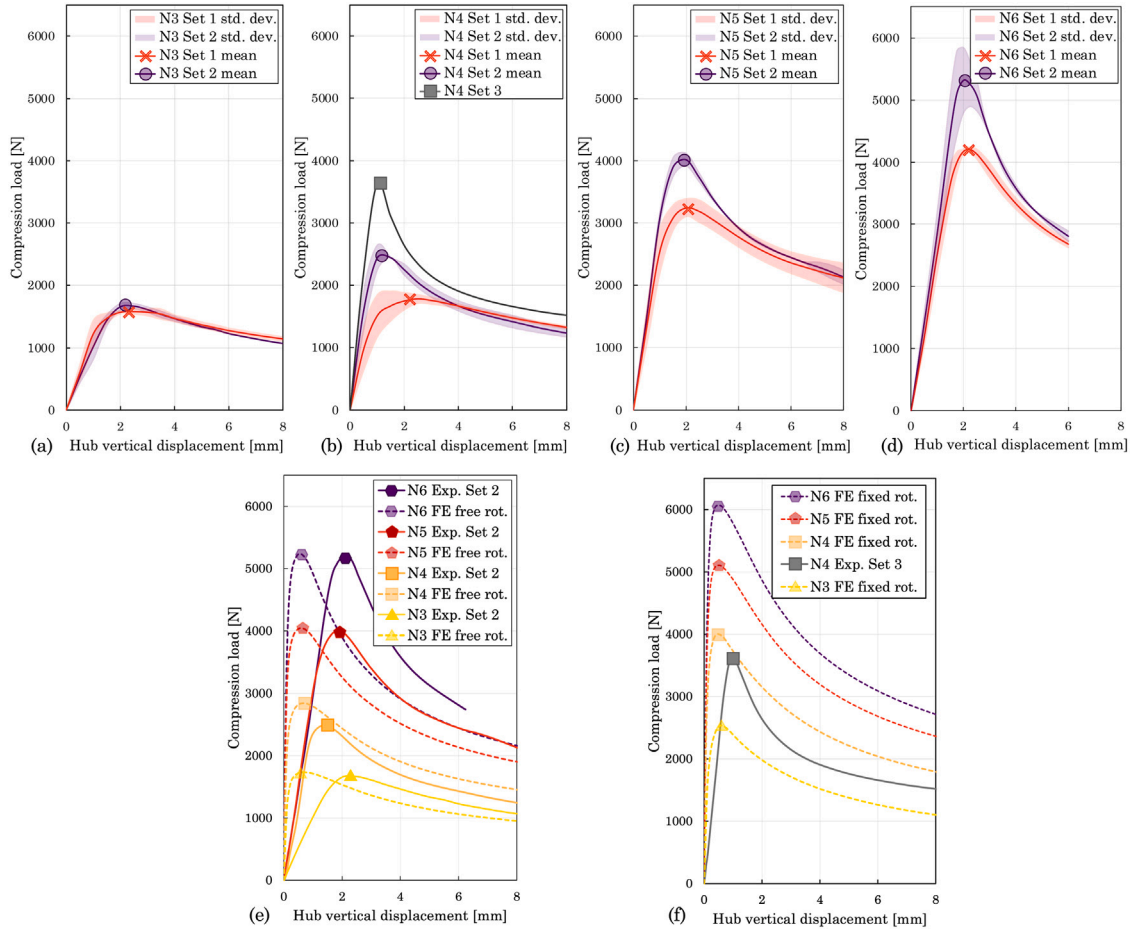

Fig. 11. Equilibrium paths obtained from Set 1 to Set 3 experimental results of (a) triangular, (b) quadrilateral, (c) pentagonal, and (d) hexagonal kirigami units; (e) Set 2 experimental results and FE simulations with free hub rotation boundary conditions; and (f) numerical FE results for fixed hub rotation boundary conditions and Set 3 experimental result.

Table 4
Buckling load ratios from experimental and FE simulation results.

Buckling load of	N3	N4	N5	N6
$\frac{\text{Set 2}}{\text{Set 1}}$	10%	40%	23%	24%
$\frac{\text{FE free rot.–Set 2}}{\text{FE free rot.}}$	4%	13%	1%	1%
$\frac{\text{FE Fixed rot.}}{\text{FE Free rot.}}$	46%	40%	26%	16%
$\frac{\text{Set 2}}{\text{Deploy load}}$	15	17	13	14

were simulated and tested. In the first group of FE models ("FE free rot".) the hub was compressed and allowed to rotate freely about the vertical axis (z axis). This boundary condition reflected the experimental setup for testing specimens grouped under Set 2. In the second group of models ("FE fixed rot".) the hub was restricted to rotate about the vertical axis, allowing only its vertical displacement, matching the testing conditions of Set 3.

Results plotted in Fig. 11(e) show that the free rotation FE models predicted buckling loads in close agreement with the Set 2 experiments of all polygonal shapes. Additionally, Table 4 shows the difference between the results of the FE models with free hub rotation and Set 2 experimental results for each polygon. The magnitude of the differences (ranging from 1% to 13%) is small and considered acceptable due to the variations of the manual fabrication process and assumptions made in generating the simulation model described in Section 2.2. The most significant difference (13%) seen for the quadrilateral units is associated with the cutting process with the water jet. Upon further inspection of the testing specimens, it was found that during fabrication, the cutting tip of the water jet was aligned to the inner side of the secondary leg curve and not centered on the provided cut pattern. This slight offset of the cutting tip produced smaller widths at the secondary leg pinched areas than the intended design, slightly reducing the buckling load capacity.

While the experimental and simulation buckling loads shown in Fig. 11(e) show good agreement, there is also a noticeable difference in the pre-buckling stiffness in all the polygonal shapes. This difference in stiffness is attributed to a combination of factors that the FE models do not capture because of the simplifications made in the model definition. One of those factors can be the definition of contact interactions between the top and bottom compression plates. The boundary conditions in the FE model create an apparent optimum contact for load transmission that may not be present in the experimental units. The combination of this factor, plus the possible presence of other geometric imperfections in the kirigami units themselves, results in lower pre-buckling stiffness than the stiffness predicted by the FE models. Despite this limitation, the models can predict the peak compression load, which is this study's main quantity of interest.

Fig. 11(f) shows the equilibrium paths and buckling loads obtained assuming a fixed rotation hub boundary condition for the FE simulations of all polygons. The increase of buckling loads with respect to values shown in Fig. 11(e) ranged from 46% (N3) to 16% (N6) (see Table 4). Additionally, Set 3 experimental results in Figs. 11(b) and 11(f) showed a similar increase in buckling load to those predicted by the FE analyses. The buckling load difference between N4 fixed rotation FE model and Set 3 experimental results is 9.4%, similar to that of the N4 in free rotation and Set 2 (13%). The increase in buckling load

between fixed and free hub rotation for the experimental results (Set 3/Set 2) is 45%, a value similar to that of the FE results (40%). This similarity indicates that the FE models with fixed hub rotations are reliable for buckling load predictions.

This set of results comparing the boundary conditions suggest that polygons with more edges are less susceptible to changes in hub boundary conditions for compression loads. However, the same trend does not continue when comparing the buckling-to-deployment load ratio of each polygon. Table 4 shows the buckling-to-deployment load ratio of Set 2. Units with fewer edges presented higher buckling-to-deployment load ratios (15 and 17 for N3 and N4, respectively), while units with more edges presented lower ratios (13 and 14 for N5 and N6, respectively). These results suggest that polygons with more edges have higher buckling capacity than those with fewer edges; however, they also require a higher force input for initial hub deployment.

Load magnitudes cannot be directly compared between the present work and literature [27] given the different manufacturing reasons provided in Section 3.1. Nevertheless, load ratios may be compared for quadrilateral units. Set 3 buckling-to-deployment ratio (N4) is 24, the same value reported in [27]. Set 3 is considered to have the same boundary conditions and similar secondary leg curvature bending radius as presented in the specimens reported in [27]. Additionally, the post-buckling load–displacement trajectories of experiments [27] show a sudden loss of load-carrying capacity, associated with cracks of welded joints. This result differs from the present work, with a smooth nonlinear post-buckling equilibrium path that remained consistent for all tested specimens.

Finally, Figs. 11(e) and 11(f) show that the slopes of the pre-buckling equilibrium paths predicted by the FE models are steeper than those produced by experiments. As mentioned previously, the slightly less inclined slopes obtained from the experiments are attributed to a combination of factors such as contact interactions and geometric imperfections that the FE models cannot capture directly from the model generation sequence described in Section 2.2. The possible sources of imperfections observed during the experimental phase include local warping resulting from the welding process, local geometric irregularities from secondary leg bending, and consistency during manual manufacturing procedures such as placement or alignment of the secondary leg endpoint for welding. A precise quantification of the geometric differences between post-fabrication and pre-testing experimental specimens vs. FE models would require point to point precise measurements that are beyond the scope of the current investigation.

3.2.3. Hub rotation

Section 3.1 showed that the hub of kirigami units rotated in the range of 28° to 36° in the counterclockwise direction during the deployment step (Table 3). The hub rotations around the vertical axis (z axis) were also measured during the compression tests. This measurement quantifies the hub rotation that the kirigami units can withstand before buckling. Rotation measurements indicated that, at the buckling load, hubs rotated less than 2° in the clockwise direction, as summarized in Table 5. Table 5 also summarizes the rotations predicted by the FE models (UR3) of each polygon corner. Both experimental and FE models resulted in similar rotation values of less than 1 degree, except for N3 experimental units with an average of 1.5 degrees, which were affected by the slight distortion of the hub corners (see Fig. 10(c)) while in contact with the compression plate. These results confirm that the FE models are a reliable representation of physical experiments.

A closer look at the values summarized on Table 5 indicates that all units from Set 2 presented smaller hub rotations than Set 1. This result suggests that the modifications introduced in the manufacturing of Set 2 specimens straightened the transition between secondary legs and hub. This straightening increased the axial and rotational stiffness of the unit. A stiffer structure resulted in smaller rotations and a larger compression load-carrying capacity, as shown in Fig. 11.

Table 5
Hub rotations at the onset of buckling load, experimental and FE simulation results.

N	Average Experimental [deg]			FE simulation [deg]
	Set 1	Set 2	All specimens	Avg. UR3 N corners
3	1.7	1.3	1.5	0.6
4	0.8	0.3	0.6	0.4
5	0.7	0.5	0.6	0.6
6	0.3	0.2	0.3	0.5

3.2.4. Buckling modes

Fig. 12 presents a sequence of images showing the pre- and post-buckling modes captured during the experiments for a quadrilateral (Fig. 12(a)) and hexagonal (Fig. 12(b)) units and their corresponding buckling modes predicted by the FE nonlinear analysis. We include a video comparing experimental and numerical results for the compression of one N6 unit in the supplemental materials. In Fig. 12, the first column of images shows the undeformed kirigami at the beginning of the compression sequence; the second shows the shape at the onset of buckling; the third shows the deflected shape of the secondary legs immediately after buckling; and the fourth shows the advanced post-buckling configuration. Deformations for experimental and FE simulations with free hub rotation models matched for all steps. Both experimental and simulation results show that the buckling hinges formed below the yielded portion of the secondary legs (shown in the stress contour of Fig. 14(b)). This result is explained by two factors: (1) the strain hardening of steel in the transition between the secondary legs and the hub; and (2) the increased rotational stiffness provided by the welded joint near the boundary polygon base and the plastic hinge near the hub. Similar results were obtained for the other polygonal units with free hub rotation.

The buckling mode of the quadrilateral kirigami units tested experimentally [27] was similarly governed by secondary leg buckling. The secondary legs buckled at approximately one-quarter of the leg length from the hub – a buckling mode consistent with those shown in the present work (Fig. 14).

The geometric design of the kirigami units tested in the present work included pinched areas created to provide weakened cross-sections to control the position of plastic hinge formation during the system deployment. The formed plastic hinges presented areas with higher stress capacity due to the strain-hardening properties of steel. Consequently, the post-buckling behavior of the kirigami units under compression loads shows that new hinges develop on the boundaries between the yielded and non-yielded portions of the secondary legs. Therefore, the results of this study show that the behavior of rotational kirigami systems is governed by the coupled effect of specific material behavior and fine-tuned geometric design.

3.2.5. Influence of the radius of secondary leg bending curvature at the leg-hub surface interface

A parametric study was conducted to study the effect of the secondary leg bending curvature near the hub on the buckling load of the kirigami units. We address only the out-of-straightness imperfection sensitivity analysis. This study includes the square unit under fixed and free hub boundary conditions. The prescribed rotation described in the model generation for the FE analysis (Section 2.2, Step 3) was applied at different distances from the pinched area in the secondary leg to produce different bending curvatures. The different distances are expressed in terms of the steel sheet thickness (see Section 2.2).

Fig. 13(a) shows that a concentrated rotation applied at $4t$ distance from the pinched area produced a radius of curvature of $R = 1.31t$. Similarly, an $8t$ distance produced a radius of $1.48t$, a $16t$ distance produced a radius of $1.63t$, and distances of $32t$ to $55t = \ell_s$ (i.e., length of the secondary legs) produced a radius of $1.81t$. The prescribed rotation locations increased quadratically, while the resulting radius of

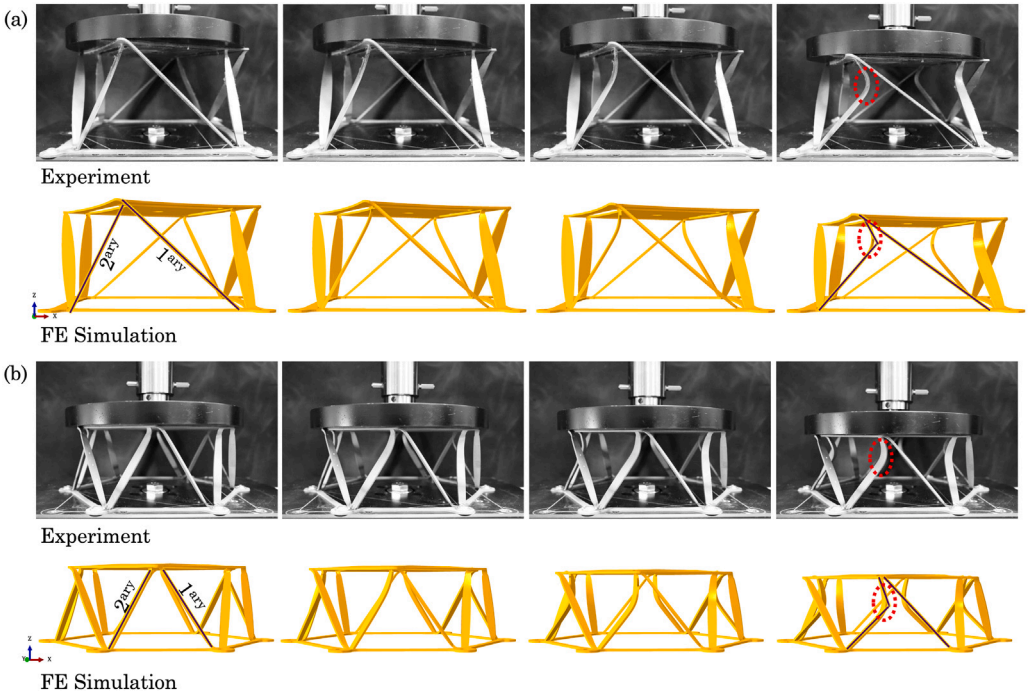

Fig. 12. Examples of buckling modes for (a) N4 and (b) N6 units.

curvature increased linearly up to $32t$. After $32t$, the prescribed rotation location had a minor impact on the resulting radius of curvature.

Figs. 13(b) (free hub rotation) and 13(c) (fixed hub rotation) present the equilibrium paths predicted by the FE models for the different radii of curvatures. For both boundary conditions, results show a noticeable decrease in the buckling load when the bending distance increases from $4t$ to $8t$, or equivalently, an increase in the radius of curvature from $1.31t$ to $1.48t$. After that point, the reduction in buckling load is not significant. Results in Figs. 13(b) and 13(c) also show that the simulation results predicted buckling loads comparable to experimental results corresponding to Set 2 and Set 3 for free and fixed hub rotation, respectively. These two sets of experimental units were manufactured with a decreased radius of curvature in the transition between the secondary legs and the hub, which allowed them to increase their compression load-carrying capacity.

Fig. 13(d) shows an imperfection sensitivity plot as a function of the bending distance and normalized buckling load for each type of boundary condition. The sensitivity curves indicate that for a fixed hub, an increase in the bending distance up to $8t$ produced a decrease in the buckling load of about 5%, while in the free-to-rotate hub, the reduction was around 13%. Higher bending distances did not significantly decrease the buckling load for both boundary conditions. These results, along with the results on the effect of changes in hub boundary conditions, indicate that rotational kirigami units are more sensitive to the boundary conditions during compression (hub free to rotate vs. hub fixed) than to changes in the radius of curvature of the transition between secondary legs and hub. Despite this difference in sensitivity, the parametric FE study shows that higher buckling loads are achievable by reducing the magnitude of the transition radius of curvature to values smaller than $1.5t$.

3.2.6. Stress analysis

Fig. 14 shows simulation results of von Mises stresses and regions of active yielding and the corresponding perspective view of the post-buckled shape from Set 2 experimental results. Fig. 14(a) shows top views of the stress concentrations on the pinched areas of both primary and secondary legs and in the transitions between the boundary polygon and hub. A closer look at the stress distribution of units N3 and N4 indicates that the primary legs are less stressed than those of units N5 and N6.

However, the side views of Fig. 14(b) show a more apparent distinction between the primary and secondary legs with regions reaching or exceeding the yielding stress. The secondary legs present a greater fraction of their length with stresses on or above the yielding limit than the primary legs. Specifically, units N3 and N4 showed higher concentrations of yielding stresses on the secondary legs with respect to the adjacent primary legs. On the other hand, units N5 and N6 presented a more even distribution of yielding stresses between primary and secondary legs compared to units N3 and N4. This difference in yielding stress distribution reflects the effect of the resulting triangulation between three components: the primary leg, the secondary leg, and the boundary polygon edge. The secondary legs of N3 units were positioned closer to a vertical position (z axis), directing the force flow to those legs. N5 and N6 units presented triangulated shapes closer to isosceles triangulated units that distribute the forces more evenly between primary and secondary legs. Section 4 elaborates on future parametric studies to understand the effect of the resulting leg triangulation on the buckling loads.

The hardening effect of the yielded steel material is evident in the post-buckled shape shown in Figs. 14(c) and 14(d). Fig. 14(c) shows active yielding in the post-buckled configuration, matching Fig. 14(d) perspectives for direct comparison. The hardened portion of the secondary legs suffered little to no deformations. The newly formed hinge was concentrated in the region immediately below the yielded area depicted in Fig. 14(b). This result is observed in the post-buckled shapes of FE simulations (Fig. 14(c)) and experimental results (Fig. 14(d)), where secondary legs were highly deformed (identified by red dotted circles), and primary legs had no visual signs of large deformations. The welded points between the secondary leg endpoint and the boundary polygon base successfully fixed the tip of the secondary legs on the boundary polygon surface. The secondary legs deformed the most at approximately one-quarter of the leg length distance from the hub surface. This buckling mode shows the secondary legs controlled the collapse behavior of the units when the hub was free to rotate.

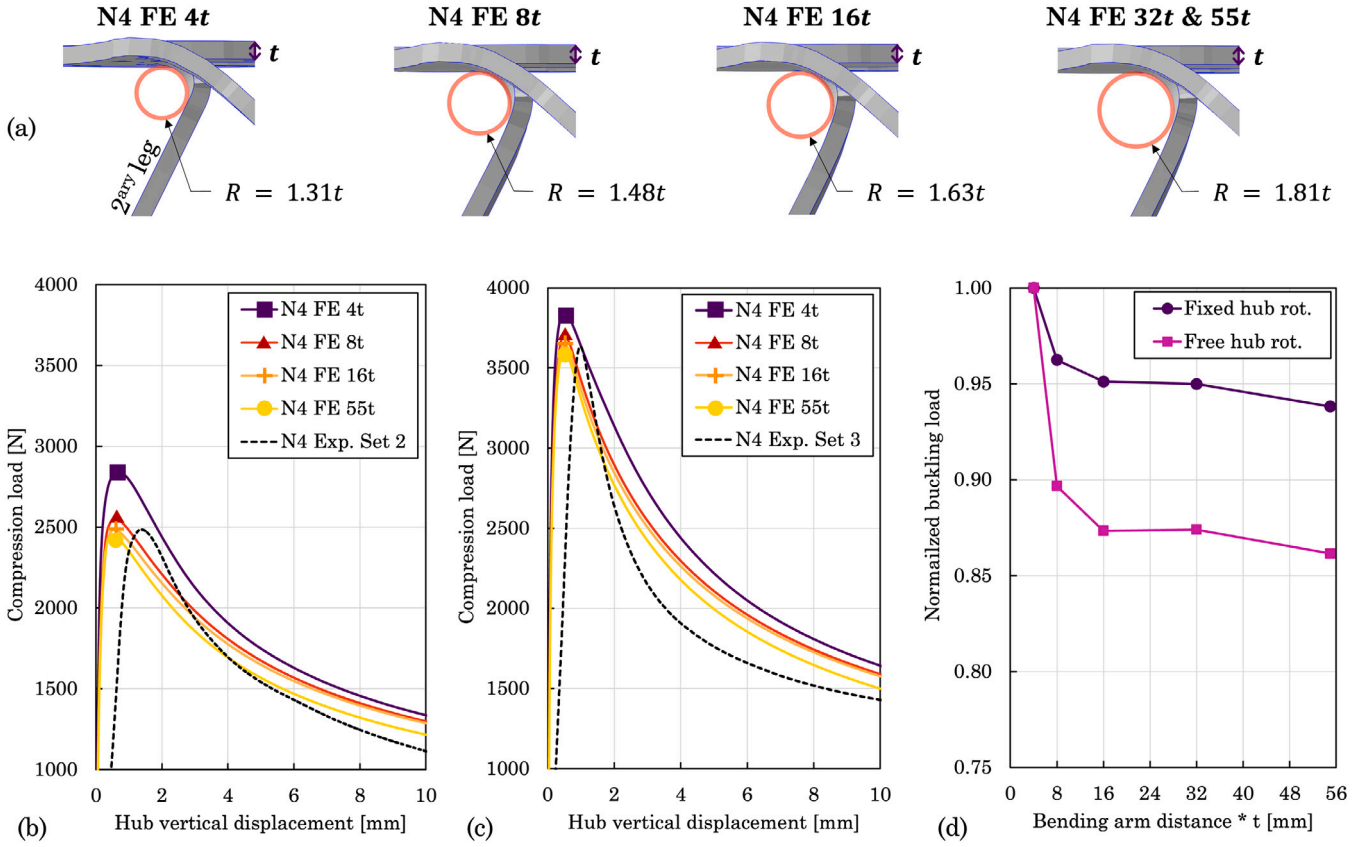

Fig. 13. Imperfection sensitivity study for unit N4: (a) Variation of transition radius of curvature R as a function of bending arm distance; (b) Equilibrium paths for different bending arm distances and free hub ratio; (c) Equilibrium paths for different bending arm distances and fixed hub rotation; (d) Imperfection sensitivity for normalized buckling loads for free and fixed hub rotation.

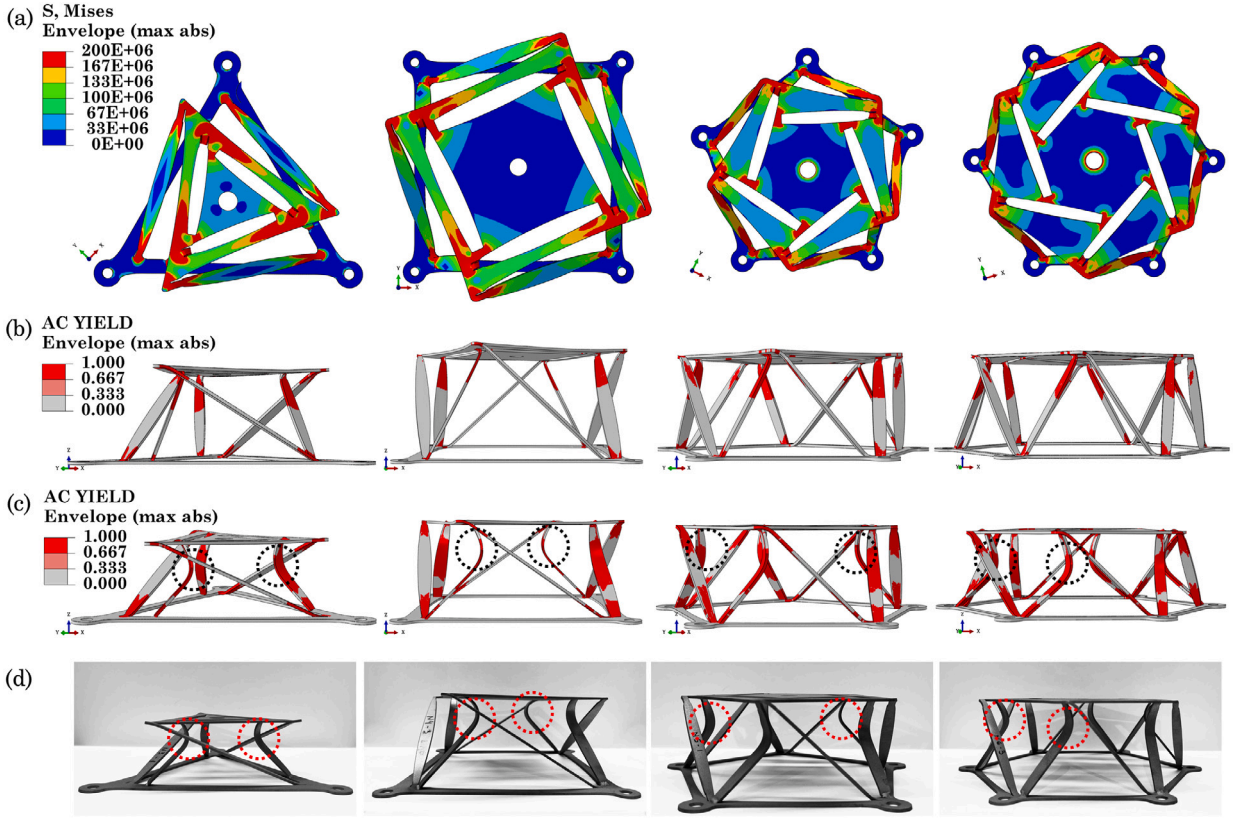

Fig. 14. Compression test results for units from N3 to N6: (a) von Mises stress contours; (b) contour of active yielding regions (von Mises stress > 186 MPa) from FE analysis at the onset of buckling and (c) in advanced post-buckled mode; and (d) post-buckled deflected shape from experiments.

4. Challenges and future work

In the present work, we investigated the mechanical response of rotational kirigami units under tension (deployment) and compression (fully deployed configuration). We studied four polygonal units (N3 to N6) with a predetermined set of cut parameters for each unit and performed a parametric study to evaluate the effect of changing the deployment method of secondary legs on the buckling load of the unit.

The deployment of all polygonal units successfully generated the intended shape, given a concentrated load at the center of the hub. However, other deployment methods that would require smaller force magnitudes will be explored in future work. For example, deploying one hub vertex at a time, as shown in [39], can be just as successful and require smaller force input. Adding a rotational motion about the vertical axis coupled to the vertical hub displacement may be another way to deploy the hubs with smaller force magnitudes.

We found that units with more primary legs (N5 and N6) take double the deployment load of units with fewer legs (N3 and N4). However, we are limited to drawing further conclusions on deployment efficiency due to slight differences in the dimensions of each unit. For example, quadrilateral units could have had a smaller deployment load than pentagons due to the quadrilaterals' longer legs, which provided a bigger lever arm to form hinges in the pinched areas. Systematic scaling studies accompanied by sensitivity analyses are necessary to draw further conclusions on the effect of each geometric parameter on the deployment and buckling loads of this system.

We noted that units with smaller secondary leg geometric imperfections, such as localized secondary leg bending curvature (Set 2), presented higher buckling loads than units with more imperfections (Set 1), as expected. We also noted that Set 2 to Set 1 buckling load ratios differ between polygonal units. That is, the load capacity increase is not uniform across different polygonal units. The varying primary to secondary leg length ratios as well as the leg inclination can explain this nonuniform increase. The study of the effect of primary to secondary leg length ratio and influence of the leg angle in the triangulated shapes on the buckling load requires a systematic parametric study that falls beyond the scope of the present work, and will be conducted in future work.

Units with fewer edges presented higher buckling-to-deployment load ratios, while units with more edges presented lower ratios. This result suggests that polygons with more edges present higher buckling capacity than those with fewer edges, requiring higher force input to manufacture. This ratio will be an essential metric in future work to optimize geometric parameters of units that require less force to manufacture while presenting higher buckling capacity.

The present work developed unique Abaqus [32] models for predetermined cut parameters as described in Section 2.2. This work was fundamental in providing FE models that reliably capture the mechanics of physical experiments (Section 3). We used standard manual modeling features to update FE models each time we iterated over different geometric parameters. Future work will include an automated workflow from the geometric cut pattern generation to the analysis of relevant numerical output. Such automation will allow systematic parametric studies of this system and a more comprehensive system characterization.

Ultimately, single units may present limitations for large-scale projects due to avoidable fabrication steps when using the multi-unit, space frame system [7]. Studying multi-unit systems is a challenging part of future work, given the many different tiling possibilities and the necessity for a larger-scale numerical model. That is, more shell elements will be required to perform a detailed structural analysis of the frames, which incurs longer computational time. The initial study of single-unit systems of the present work will allow a smoother transition to multi-unit systems and the further development of the rotational kirigami system. Such development could enable the use of this system for practical purposes, including civil engineering applications such as slabs and walls.

5. Conclusions

We have presented the experimental and numerical characterization of rotational kirigami units from unit deployment under tensile loading to units in their fully deployed configuration under compression loading. The given cut patterns range from regular triangles (N3) to hexagons (N6). The provided numerical FE models were shown to predict experimental results robustly. We presented a reproducible manufacturing method for the single-unit system and provided material characterization of the A1008 steel utilized for manufacturing the kirigami units. The presented numerical and experimental studies allow us to draw several conclusions.

1. Pinched areas are effective in forming localized plastic hinges for A1008 steel during deployment of kirigami units.
2. The force required to deploy the central hub increased as the number of primary legs connected to the central hub increased.
3. The buckling load of the kirigami units ranged from 10 to 25 times the load required to deploy the system.
4. For the geometric configurations selected for this study, the buckling modes of kirigami units showed that secondary legs control the buckling behavior of the presented system.
5. Units with fixed in-plane hub rotations had 16% to 46% increase in buckling capacity for different polygonal units compared to units with free in-plane hub rotations.
6. Reduction of geometric imperfections in secondary legs resulted in a 10% to 40% increase in buckling load capacity for different polygonal units.
7. A sensitivity study was conducted to learn about the effect of the secondary leg bending curvature near the hub on the buckling load of the kirigami units for fixed and free hub rotation boundary conditions. Simulation results indicated that rotational kirigami units are more sensitive to the boundary conditions during compression (hub free to rotate vs. hub fixed) than to changes in the radius of curvature of the transition between secondary legs and hub. Despite this difference in sensitivity, the parametric FE study showed that higher buckling loads are achievable by reducing the magnitude of the transition radius to values smaller than 1.5 times the thickness of the sheet.

CRediT authorship contribution statement

Isabel M. de Oliveira: Writing – review & editing, Writing – original draft, Visualization, Methodology, Formal analysis, Data curation, Conceptualization. **Eduardo M. Sosa:** Writing – review & editing, Writing – original draft, Validation, Resources, Methodology, Formal analysis. **Emily Baker:** Writing – review & editing, Conceptualization. **Sigrid Adriaenssens:** Writing – review & editing, Supervision, Funding acquisition.

Declaration of competing interest

The authors declare that they have no known competing financial interests or personal relationships that could have appeared to influence the work reported in this paper.

Data availability

Data will be made available on request

Acknowledgments

The first and last authors acknowledge funding provided by National Science Foundation Institute for Data-Driven Dynamical Design, Office of Advanced Cyberinfrastructure (OAC): #2118201. The bending tool was fabricated by Eder Medina from the Laboratory for Intelligent Probabilistic Systems at Princeton University. Specimen manufacturing was performed at the West Virginia University (WVU) Lane Innovation Hub. Their assistance is gratefully acknowledged. Experimental evaluations were conducted in the WVU Department of Mechanical and Aerospace Engineering labs. The assistance provided by Quinn Dugger, undergraduate research assistant under the WVU Research Apprentice Program (WVU-RAP), is also gratefully acknowledged.

Appendix A. Supplementary data

Supplementary material related to this article can be found online at https://doi.org/10.1016/j.tws.2023.111123.

References

[1] M. Meloni, J. Cai, Q. Zhang, D. Sang-Hoon Lee, M. Li, R. Ma, T.E. Parashkevov, J. Feng, Engineering origami: A comprehensive review of recent applications, design methods, and tools, Adv. Sci. 8 (13) (2021) 2000636.

[2] D.P. Holmes, Elasticity and stability of shape-shifting structures, Curr. Opin. Colloid Interface Sci. 40 (2019) 118–137.

[3] X. Ning, X. Wang, Y. Zhang, X. Yu, D. Choi, N. Zheng, D.S. Kim, Y. Huang, Y. Zhang, J.A. Rogers, Assembly of advanced materials into 3D functional structures by methods inspired by origami and Kirigami: A review, Adv. Mater. Interf. 5 (13) (2018) 1800284.

[4] J. Tao, H. Khosravi, V. Deshpande, S. Li, Engineering by cuts: How Kirigami principle enables unique mechanical properties and functionalities, Adv. Sci. 10 (1) (2023) 2204733.

[5] X. Zhang, L. Medina, H. Cai, V. Aksyuk, H.D. Espinosa, D. Lopez, Kirigami engineering–nanoscale structures exhibiting a range of controllable 3D configurations, Adv. Mater. 33 (5) (2021) 2005275.

[6] H. Lalvani, X-structures, Milgo experiment 3 (2008–2014), in: Inspiring the Next Generation - Proceedings of the International Conference on Spatial Structures 2020/21, Spatial Structures Research Centre of the University of Surrey, Surrey, 2022, pp. 3177–3189, http://dx.doi.org/10.15126/900337.

[7] E. Baker, Search for a rooted aesthetic: study in spin-valence, in: Fabricate 2014: Negotiating Design & Making, UCL Press, 2014, pp. 128–135, http://dx.doi.org/10.2307/j.ctt1tp3c5w, arXiv:10.2307/j.ctt1tp3c5w.

[8] United Structure Solution, Morris street pedestrian bridge, 2019, https://www.ussgroups.com/projects/morris-street-pedestrian-bridge.

[9] M. Ramirez, E. Baker, E. Harriss, G. Herning, Double-curved spin-valence: Geometric and computational basis, in: AAG 2020, Paris, 2020, pp. 408–425.

[10] M. Redoutey, A. Roy, E.T. Filipov, Pop-up Kirigami for stiff, dome-like structures, Int. J. Solids Struct. 229 (2021) 111140.

[11] K. Sempuku, T. Tachi, Self-folding rigid origami based on auxetic Kirigami, in: Inspiring the Next Generation - Proceedings of the International Conference on Spatial Structures 2020/21, Spatial Structures Research Centre of the University of Surrey, Surrey, 2022, pp. 3496–3507.

[12] P.M. Reis, F. López Jiménez, J. Marthelot, Transforming architectures inspired by origami, Proc. Natl. Acad. Sci. 112 (40) (2015) 12234–12235.

[13] E.T. Filipov, T. Tachi, G.H. Paulino, Origami tubes assembled into stiff, yet reconfigurable structures and metamaterials, Proc. Natl. Acad. Sci. 112 (40) (2015) 12321–12326.

[14] A. Lamoureux, K. Lee, M. Shlian, S.R. Forrest, M. Shtein, Dynamic Kirigami structures for integrated solar tracking, Nature Commun. 6 (1) (2015) 8092.

[15] S. Seon, K. Kim, C. Bae, W. Yi, A study on shock absorption characteristics of honeycomb-inserted bollards, Appl. Sci. 10 (9) (2020) 3014.

[16] Z. Chang, T.D. Ta, K. Narumi, H. Kim, F. Okuya, D. Li, K. Kato, J. Qi, Y. Miyamoto, K. Saito, Y. Kawahara, Kirigami haptic swatches: design methods for cut-and-fold haptic feedback mechanisms, in: Proceedings of the 2020 CHI Conference on Human Factors in Computing Systems, ACM, Honolulu HI USA, 2020, pp. 1–12, http://dx.doi.org/10.1145/3313831.3376655.

[17] A. Eda, H. Yasuga, T. Sato, Y. Sato, K. Suto, T. Tachi, E. Iwase, Large curvature self-folding method of a thick metal layer for hinged origami/Kirigami stretchable electronic devices, Micromachines 13 (6) (2022) 907.

[18] Y. Hong, Y. Chi, S. Wu, Y. Li, Y. Zhu, J. Yin, Boundary curvature guided programmable shape-morphing Kirigami sheets, Nature Commun. 13 (1) (2022) 530.

[19] H. Lalvani, Expanded surfaces: XURF, Milgo experiment 2 (1998–2010), in: Inspiring the Next Generation - Proceedings of the International Conference on Spatial Structures 2020/21, Spatial Structures Research Centre of the University of Surrey, Surrey, 2022, pp. 3163–3176, http://dx.doi.org/10.15126/900337.

[20] H. Lalvani, Form-making and industrial production: algorithms, Milgo experimento 1 (1997–2004), in: Inspiring the Next Generation - Proceedings of the International Conference on Spatial Structures 2020/21, Spatial Structures Research Centre of the University of Surrey, Surrey, 2022, pp. 3149–3162, http://dx.doi.org/10.15126/900337.

[21] Y. Li, Q. Zhang, Y. Hong, J. Yin, 3D transformable modular Kirigami based programmable metamaterials, Adv. Funct. Mater. 31 (43) (2021) 2105641.

[22] A. English, Flat-pack future, Land J. (2019) 21, Copyright - Copyright Royal Institution of Chartered Surveyors Jul/Aug 2019; Last updated - 2019-08-28.

[23] Y. Miyamoto, Rotational erection system (res): Origami extended with cuts, in: Origami, American Mathematical Society, Providence, Rhode Island, 2015, pp. 537–544, http://dx.doi.org/10.1090/mbk/095.2/16.

[24] T. Yoneda, Y. Miyamoto, H. Wada, Structure, design, and mechanics of a pop-up origami with cuts, Phys. Rev. A 17 (2) (2022) L021004.

[25] Q. Zhang, N. Pan, J. Cai, J. Feng, Programmable and reconfigurable surfaces with Kirigami-inspired bistable elements, J. Int. Assoc. Shell Spatial Struct. 62 (4) (2021) 262–270.

[26] N. Sherrow-Groves, E. Baker, Structural finite-element analysis of steel Kirigami space frame to characterize global behavior, in: International Centre for Numerical Methods in Engineering, CIMNE, International Centre for Numerical Methods in Engineering (CIMNE), Barcelona, 2019, pp. 1757–1764.

[27] J. Sahuc, G.M. Herning, E. Baker, Experimental and analytical investigation of the spin-valence Kirigami space frame, in: Form and Force, International Centre for Numerical Methods in Engineering (CIMNE), Barcelona, 2019, pp. 1733–1740.

[28] S. Timoshenko, S. Woinowsky-Krieger, Theory of Plates and Shells, in: Engineering Mechanics Series, McGraw-Hill, 1959.

[29] R.C. Hibbeler, Structural Analysis, Tenth edition, Pearson, New York, NY, 2018.

[30] W.F. Baker, L.L. Beghini, A. Mazurek, J. Carrion, A. Beghini, Structural innovation: Combining classic theories with new technologies, Eng. J. 52 (2015) 203–217.

[31] Robert McNeel & Associates, Rhinoceros3d, 2007, URL https://www.rhino3d.com/.

[32] Dassault Systemes Simulia Corp., Abaqus User's Manual, Documentation Collection, Version 2022, Johnston, 2022.

[33] ASM International, Atlas of Stress-Strain Curves, Second Ed., ASM International, 2002.

[34] G.J. Simitses, D.H. Hodges, Fundamentals of Structural Stability, Elsevier/Butterworth-Heinemann, Amsterdam, Boston, 2006.

[35] J. Croll, Comments on effective use of numerical modelling and extended classical shell buckling theory, Proc. R. Soc. A: Math. Phys. Eng. Sci. 479 (2269) (2023) 20220622.

[36] H. Wagner, E. Sosa, T. Ludwig, J. Croll, C. Hühne, Robust design of imperfection sensitive thin-walled shells under axial compression, bending or external pressure, Int. J. Mech. Sci. 156 (2019) 205–220.

[37] S. Timoshenko, J.M. Gere, Theory of Elastic Stability, Second ed., Dover ed., Dover Publications, Mineola, N.Y, 2009.

[38] R.C. Hibbeler, Mechanics of Materials, Pearson, 2016.

[39] J. Sahuc, Experimental and Analytical Investigation of the Spin-Valence Kirigami Space Frame (M.Eng. thesis), Massachusetts Institute of Technology, 2019.